

**Traces of nonequilibrium dynamics in relativistic heavy-ion collisions**Yingru Xu,<sup>1,\*</sup> Pierre Moreau,<sup>2,3,4</sup> Taesoo Song,<sup>2,3,5</sup> Marlene Nahrgang,<sup>1,6</sup> Steffen A. Bass,<sup>1</sup> and Elena Bratkovskaya<sup>3,4</sup><sup>1</sup>*Department of Physics, Duke University, Durham, North Carolina 27708, USA*<sup>2</sup>*Frankfurt Institute for Advanced Studies, Johann Wolfgang Goethe Universität, D-Frankfurt am Main, Germany*<sup>3</sup>*Institute for Theoretical Physics, Johann Wolfgang Goethe Universität, D-Frankfurt am Main, Germany*<sup>4</sup>*GSI Helmholtzzentrum für Schwerionenforschung GmbH, Planckstrasse 1, D-64291 Darmstadt, Germany*<sup>5</sup>*Institut für Theoretische Physik, Universität Gießen, Heinrich-Buff-Ring 16, D-35392 Gießen, Germany*<sup>6</sup>*SUBATECH UMR 6457 (IMT Atlantique, Université de Nantes, IN2P3/CNRS), 4 Rue Alfred Kastler, F-44307 Nantes, France*

(Received 27 March 2017; published 8 August 2017)

The impact of nonequilibrium effects on the dynamics of heavy-ion collisions is investigated by comparing a nonequilibrium transport approach, the Parton-Hadron-String-Dynamics (PHSD), to a 2D+1 viscous hydrodynamical model, which is based on the assumption of local equilibrium and conservation laws. Starting the hydrodynamical model from the same nonequilibrium initial condition as in the PHSD, using an equivalent IQCD equation of state (EoS), the same transport coefficients, i.e., shear viscosity  $\eta$  and the bulk viscosity  $\zeta$  in the hydrodynamical model, we compare the time evolution of the system in terms of energy density, Fourier transformed energy density, spatial and momentum eccentricities, and ellipticity to quantify the traces of nonequilibrium phenomena. In addition, we also investigate the role of initial pre-equilibrium flow on the hydrodynamical evolution and demonstrate its importance for final state observables. We find that because of nonequilibrium effects, the event-by-event transport calculations show large fluctuations in the collective properties, while ensemble averaged observables are close to the hydrodynamical results.

DOI: [10.1103/PhysRevC.96.024902](https://doi.org/10.1103/PhysRevC.96.024902)**I. INTRODUCTION**

Relativistic heavy-ion collisions produce a hot, dense phase of strongly interacting matter commonly known as the quark-gluon plasma (QGP) which rapidly expands and freezes into discrete particles [1–7]. Because the QGP is not directly observable—only final-state hadrons and electromagnetic probes are detected—present research relies on dynamical models to establish the connection between observable quantities and the physical properties of interest. The output of these dynamical model simulations are analogous to experimental measurements as they provide final state particle distributions from which a wide variety of observables related to the bulk properties of QCD matter can be obtained. In addition, dynamical models also provide information on the full space-time evolution of the QCD medium. This information can be utilized for the study of rare probes, such as jets, heavy quarks, and electromagnetic radiation that are sensitive to the properties of the medium either via re-interaction with the QGP constituents or its production.

There exist a variety of different dynamical models, based on different transport concepts that have been successful in describing current data measured at the Relativistic Heavy-Ion Collider at Brookhaven National Laboratory and at the Large Hadron Collider at CERN. These models may differ in their assumptions on the formation of the deconfined phase of QCD matter, the nature of its dynamical evolution, the mechanism of hadron formation and freeze-out, and on many other details. A key question that needs to be addressed is how sensitive current observables are to these differences and what kind of

strategy to pursue to ascertain which of these model features reflect the actual physical nature of the hot and dense QCD system.

In this paper we perform a comparison of two prominent models for the evolution of bulk QCD matter. The first one is a nonequilibrium transport approach, the Parton-Hadron-String-Dynamics (PHSD) [8–10], and the second one a 2D+1 viscous hydrodynamical model, VISHNew [11,12] which is based on the assumption of local equilibrium and conservation laws.

Nonequilibrium effects are considered to be strongest during the early phase of the heavy-ion reaction and thus may significantly impact the properties of probes with early production times, such as heavy quarks (charm and bottom hadrons), electromagnetic probes (direct photons and dileptons), and jets. Moreover, some bulk observables, such as correlation functions and higher-order anisotropy coefficients, might also retain traces of nonequilibrium effects [13–15]. In particular, the impact of the event-by-event fluctuations on the collective observables was studied by Kodama *et al.* [14]. Based on the comparison of the coarse-grained hydrodynamical evolution with the PHSD dynamics, they find that in spite of large fluctuations on an event-by-event basis in the PHSD, the ensemble averages are close to the hydrodynamical limit. A similar behavior was pointed out before within the PHSD study in Ref. [8] where a linear correlation of the elliptic flow  $v_2$  with the initial spatial eccentricity  $\varepsilon_2$  was obtained for the model study of an expanding partonic fireball (cf. Fig. 7 in Ref. [8]). Such correlations of  $v_2$  versus  $\varepsilon_2$  are expected in the ideal hydrodynamical case [16]. The large event-by-event fluctuations of the charge distributions was addressed also in another PHSD study [17].

In the present paper our focus will be on isolating differences in the dynamical evolution of the system that can

\*yx59@phy.duke.edu

be attributed to nonequilibrium dynamics. The groundwork laid in this comparative study will hopefully lead to the development of new observables that have an enhanced sensitivity to the nonequilibrium components of the evolution of bulk QCD matter and that will allow us to quantify how far off equilibrium the system actually evolves.

## II. DESCRIPTION OF THE MODELS

### A. PHSD transport approach

The Parton-Hadron-String Dynamics (PHSD) transport approach [8–10,18] is a microscopic covariant dynamical model for strongly interacting systems formulated on the basis of Kadanoff-Baym equations [19,20] for Green’s functions in phase-space representation (in first-order gradient expansion beyond the quasiparticle approximation). The approach consistently describes the full evolution of a relativistic heavy-ion collision from the initial hard scatterings and string formation through the dynamical deconfinement phase transition to the strongly interacting quark-gluon plasma (sQGP) as well as hadronization and the subsequent interactions in the expanding hadronic phase as in the Hadron-String-Dynamics (HSD) transport approach [21]. The transport theoretical description of quarks and gluons in the PHSD is based on the Dynamical Quasi-Particle Model (DQPM) for partons that is constructed to reproduce lattice QCD results for the QGP in thermodynamic equilibrium [18,22] on the basis of effective propagators for quarks and gluons. The DQPM is thermodynamically consistent and the effective parton propagators incorporate finite masses (scalar mean fields) for gluons and quarks as well as a finite width that describes the medium dependent reaction rate. For fixed thermodynamic parameters  $(T, \mu_q)$  the partonic widths  $\Gamma_i(T, \mu_q)$  fix the effective two-body interactions that are presently implemented in the PHSD [23]. The PHSD differs from conventional Boltzmann approaches in a couple of essential aspects: (i) it incorporates dynamical quasiparticles from the finite width of the spectral functions (imaginary part of the propagators); (ii) it involves scalar mean fields that substantially drive the collective flow in the partonic phase; (iii) it is based on a realistic equation of state from lattice QCD and thus describes the speed of sound  $c_s(T)$  reliably; (iv) the hadronization is described by the fusion of off-shell partons to off-shell hadronic states (resonances or strings) and does not violate the second law of thermodynamics; (v) all conservation laws (energy momentum, flavor currents, etc.) are fulfilled in the hadronization contrary to coalescence models; (vi) the effective partonic cross sections are not given by pQCD but are self-consistently determined within the DQPM and probed by transport coefficients (correlators) in thermodynamic equilibrium. The latter can be calculated within the DQPM or can be extracted from the PHSD by performing calculations in a finite box with periodic boundary conditions (shear- and bulk viscosity, electric conductivity, magnetic susceptibility, etc. [24,25]). Both methods show a good agreement.

In the beginning of relativistic heavy-ion collisions color-neutral strings (described by the LUND model [26]) are produced in highly energetic scatterings of nucleons from

the impinging nuclei. These strings are dissolved into “pre-hadrons” with a formation time of  $\sim 0.8$  fm/c in the rest frame of the corresponding string, except for the “leading hadrons.” Those are the fastest residues of the string ends, which can re-interact (practically instantly) with hadrons with a reduced cross section in line with quark counting rules. If, however, the local energy density is larger than the critical value for the phase transition, which is taken to be  $\sim 0.5$  GeV/fm<sup>3</sup>, the pre-hadrons melt into (colored) effective quarks and antiquarks in their self-generated repulsive mean field as defined by the DQPM [18,22]. In the DQPM the quarks, antiquarks, and gluons are dressed quasiparticles and have temperature-dependent effective masses and widths which have been fitted to lattice thermal quantities such as energy density, pressure, and entropy density. The nonzero width of the quasiparticles implies the off-shellness of partons, which is taken into account in the scattering and propagation of partons in the QGP on the same footing (i.e., propagators and couplings).

The transition from the partonic to hadronic degrees of freedom (for light quarks and antiquarks) is described by covariant transition rates for the fusion of quark-antiquark pairs to mesonic resonances or three quarks (antiquarks) to baryonic states, i.e., by the dynamical hadronization. Note that because of the off-shell nature of both partons and hadrons, the hadronization process described above obeys all conservation laws (i.e., four-momentum conservation and flavor current conservation) in each event, as well as the detailed balance relations and the increase in the total entropy  $S$ . In the hadronic phase PHSD is equivalent to the hadron-strings dynamics (HSD) model [21] that was employed in the past from SchwerIonen-Synchrotron (SIS) to SPS energies. On the other hand the PHSD approach was applied to p+p, p+A and relativistic heavy-ion collisions from lower SPS to LHC energies and was successful in describing a large number of experimental data including single-particle spectra, collective flow, as well as electromagnetic probes [9,10,27,28].

### B. 2D+1 viscous hydrodynamics

Relativistic hydrodynamical models calculate the space-time evolution of the QGP medium via the conservation equations,

$$\partial_\mu T^{\mu\nu} = 0, \quad (1)$$

for the energy-momentum tensor,

$$T^{\mu\nu} = e u^\mu u^\nu - \Delta^{\mu\nu} (P + \Pi) + \pi^{\mu\nu}, \quad (2)$$

provided a set of initial conditions for the fluid flow velocity  $u^\mu$ , energy density  $e$ , pressure  $P$ , shear stress tensor  $\pi^{\mu\nu}$ , and bulk viscous pressure  $\Pi$ . For our analysis, we use VISH2+1 [11], which is an extensively tested implementation of boost-invariant viscous hydrodynamics that was updated to handle fluctuating event-by-event initial conditions [12]. We use the method from Ref. [29] for the calculation of the shear stress tensor  $\pi^{\mu\nu}$ .

This particular implementation of viscous hydrodynamics calculates the time evolution of the viscous corrections through the second-order Israel-Stewart equations [30,31] in the

14-momentum approximation, which yields a set of relaxation-type equations [32],

$$\tau_{\Pi} \dot{\Pi} + \Pi = -\zeta\theta - \delta_{\Pi\Pi}\Pi\theta + \phi_1\Pi^2 + \lambda_{\Pi\pi}\pi^{\mu\nu}\sigma_{\mu\nu} + \phi_3\pi^{\mu\nu}\pi_{\mu\nu}, \quad (3a)$$

$$\tau_{\pi}\dot{\pi}^{(\mu\nu)} + \pi^{\mu\nu} = 2\eta\sigma^{\mu\nu} + 2\pi_{\alpha}^{(\mu}w^{v)\alpha} - \delta_{\pi\pi}\pi^{\mu\nu}\theta + \phi_7\pi_{\alpha}^{(\mu}\pi^{v)\alpha} - \tau_{\pi\pi}\pi_{\alpha}^{(\mu}\sigma^{v)\alpha} + \lambda_{\pi\Pi}\Pi\sigma^{\mu\nu} + \phi_6\Pi\pi^{\mu\nu}. \quad (3b)$$

Here,  $\eta$  and  $\zeta$  are the shear and bulk viscosities. For the remaining transport coefficients, we use analytic results derived for a gas of classical particles in the limit of small but finite masses [32].

The hydrodynamical equations of motion must be closed by an equation of state (EoS),  $P = P(e)$ . We use a modern QCD EoS based on continuum extrapolated lattice calculations at zero baryon density published by the HotQCD collaboration [33] and blended into a hadron resonance gas EoS in the interval  $110 \leq T \leq 130$  MeV using a smooth step interpolation function [34]. While not identical, this EoS is compatible with the one that the DQPM model (underlying the PHSD approach) is tuned to reproduce.

To start the hydrodynamical calculation, an initial condition needs to be specified. Initial condition models provide the outcome of the collision's pre-equilibrium evolution at the hydrodynamical thermalization time, at approximately  $0.5$  fm/c. This pre-equilibrium stage is the least understood phase of a heavy-ion collision. While some hydrodynamical models explicitly incorporate pre-equilibrium dynamics [35] starting from a full initial state calculation, others sidestep the uncertainty associated with this early regime by generating parametric initial conditions directly at the materialization time [36–38].

For our study here, we shall initialize the hydrodynamical calculation with an initial condition extracted from PHSD that provides us with a common starting configuration for both models regarding our comparison of the dynamical evolution of the system.

### III. NONEQUILIBRIUM INITIAL CONDITIONS

In this section we describe the construction of the initial condition for the hydrodynamical evolution from the nonequilibrium PHSD evolution. One should note that PHSD starts its calculation *ab initio* with two colliding nuclei and makes no equilibrium assumptions regarding the nature of the hot and dense system during the course of its evolution from initial nuclear overlap to final hadronic freeze-out. For the purpose of our comparison we have to select the earliest possible time during the PHSD evolution where the system is in a state in which a hydrodynamical evolution is feasible (e.g., the viscous corrections are already small enough) and generate an initial condition for the hydrodynamical calculation at that time (note that this criterion is less stringent than assuming full momentum isotropization or local thermal equilibrium).

#### A. Evaluation of the energy-momentum tensor $T^{\mu\nu}$ in PHSD

The energy-momentum tensor  $T^{\mu\nu}(x)$  of an ideal fluid [by removing viscous corrections in Eq. (2)] is given by

$$T^{\mu\nu} = (e + P)u^{\mu}u^{\nu} - Pg^{\mu\nu}, \quad (4)$$

where  $e$  is the energy density,  $P$  the thermodynamic pressure expressed in the local rest frame (LRF), and the 4-velocity is  $u^{\mu} = \gamma(1, \beta_x, \beta_y, \beta_z)$ . Here  $\beta$  is the (3-)velocity of the considered fluid element and the associated Lorentz factor is given by  $\gamma = 1/\sqrt{1 - \beta^2}$ .

To calculate  $T^{\mu\nu}$  in PHSD which fully describes the medium in every space-time coordinate, the space time is divided into cells of size  $\Delta x = 1$  fm,  $\Delta y = 1$  fm (which is comparable to the size of a hadron) and  $\Delta z \propto 0.5 \times t/\gamma_{NN}$  scaled by  $\gamma_{NN}$  to account for the expansion of the system. We note that choosing a high resolution was shown in Ref. [27] to lead to very similar results. In each cell, we can obtain  $T^{\mu\nu}$  in

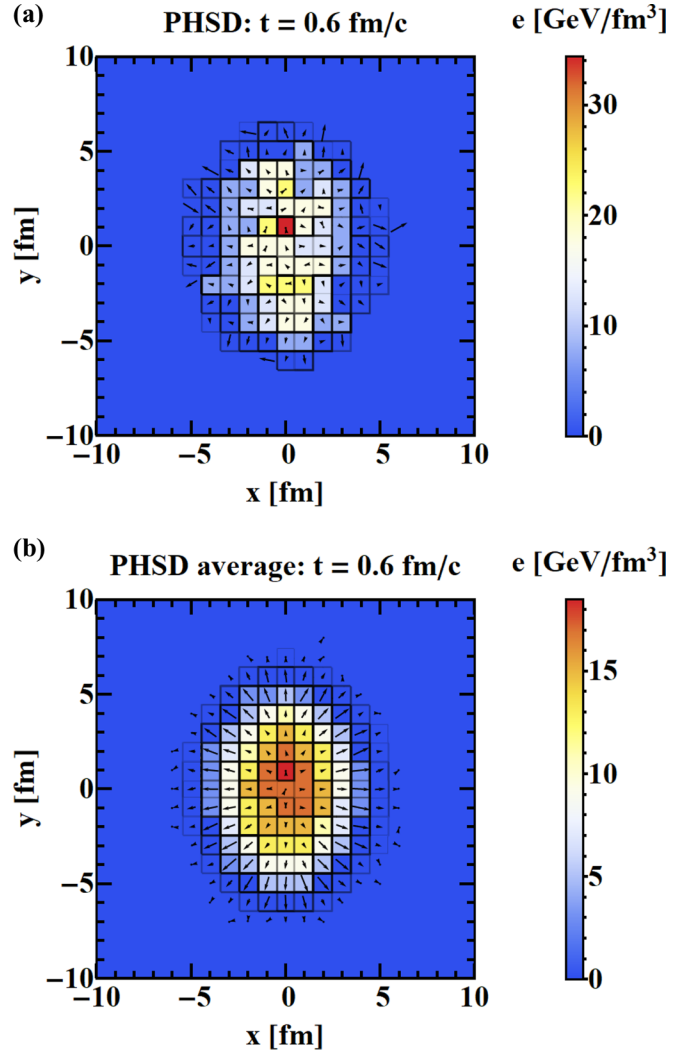


FIG. 1. Initial conditions for hydrodynamics: the energy density profiles from a single PHSD event (a) and averaged over 100 PHSD events (b) taken at  $t = 0.6$  fm/c for a peripheral ( $b = 6$  fm) Au+Au collision at  $\sqrt{s_{NN}} = 200$  GeV.

the computational frame from

$$T^{\mu\nu}(x) = \sum_i \int_0^\infty \frac{d^3 p_i}{(2\pi)^3} f_i(E_i) \frac{p_i^\mu p_i^\nu}{E_i}, \quad (5)$$

where  $f_i(E)$  is the distribution function corresponding to the particle  $i$ ,  $p_i^\mu$  the 4-momentum, and  $E_i = p_i^0$  is the energy of the particle  $i$ . In the case of an ideal fluid, if the matter is at rest [ $u^\mu = (1, 0, 0, 0)$ ]  $T^{\mu\nu}(x)$  should only have diagonal components and the energy density in the cell can be identified to the  $T^{00}$  component. However, in heavy-ion collisions the matter is viscous, anisotropic, and relativistic, thus the different components of the pressure are not equal and it becomes more difficult to extract the relevant information. This especially holds true for the early reaction time at which the initial conditions for hydrodynamical model are taken. To obtain the needed quantities ( $e, \beta$ ) from  $T^{\mu\nu}$  for the hydrodynamical evolution, we have to express them in the local rest frame (LRF) of each cell of our space-time grid. In the general case, the energy-momentum tensor can always be diagonalized, i.e., presented as

$$T^{\mu\nu}(x_\nu)_i = \lambda_i (x^\mu)_i = \lambda_i g^{\mu\nu}(x_\nu)_i, \quad (6)$$

with  $i = 0, 1, 2, 3$ , where its eigenvalues are  $\lambda_i$  and the corresponding eigenvectors  $(x_\nu)_i$ . When  $i = 0$ , the local energy density  $e$  is identified to the eigenvalue of  $T^{\mu\nu}$  (Landau matching) and the corresponding timelike eigenvector is defined as the 4-velocity  $u_\nu$  [multiplying (4) by  $u_\nu$ ]:

$$T^{\mu\nu} u_\nu = e u^\mu = (e g^{\mu\nu}) u_\nu, \quad (7)$$

using the normalization condition  $u^\mu u_\mu = 1$ . To solve this equation, we have to calculate the determinant of the corresponding matrix which is the fourth-order characteristic polynomial associated with the eigenvalues  $\lambda$ :

$$P(\lambda) = \begin{vmatrix} T^{00} - \lambda & T^{01} & T^{02} & T^{03} \\ T^{10} & T^{11} + \lambda & T^{12} & T^{13} \\ T^{20} & T^{21} & T^{22} + \lambda & T^{23} \\ T^{30} & T^{31} & T^{32} & T^{33} + \lambda \end{vmatrix}. \quad (8)$$

Having the four solutions for this polynomial, we can identify the energy density being the larger and positive solution, and the three other solutions are ( $-P_i$ ) the pressure components expressed in the LRF. To obtain the 4-velocity of the cell, we

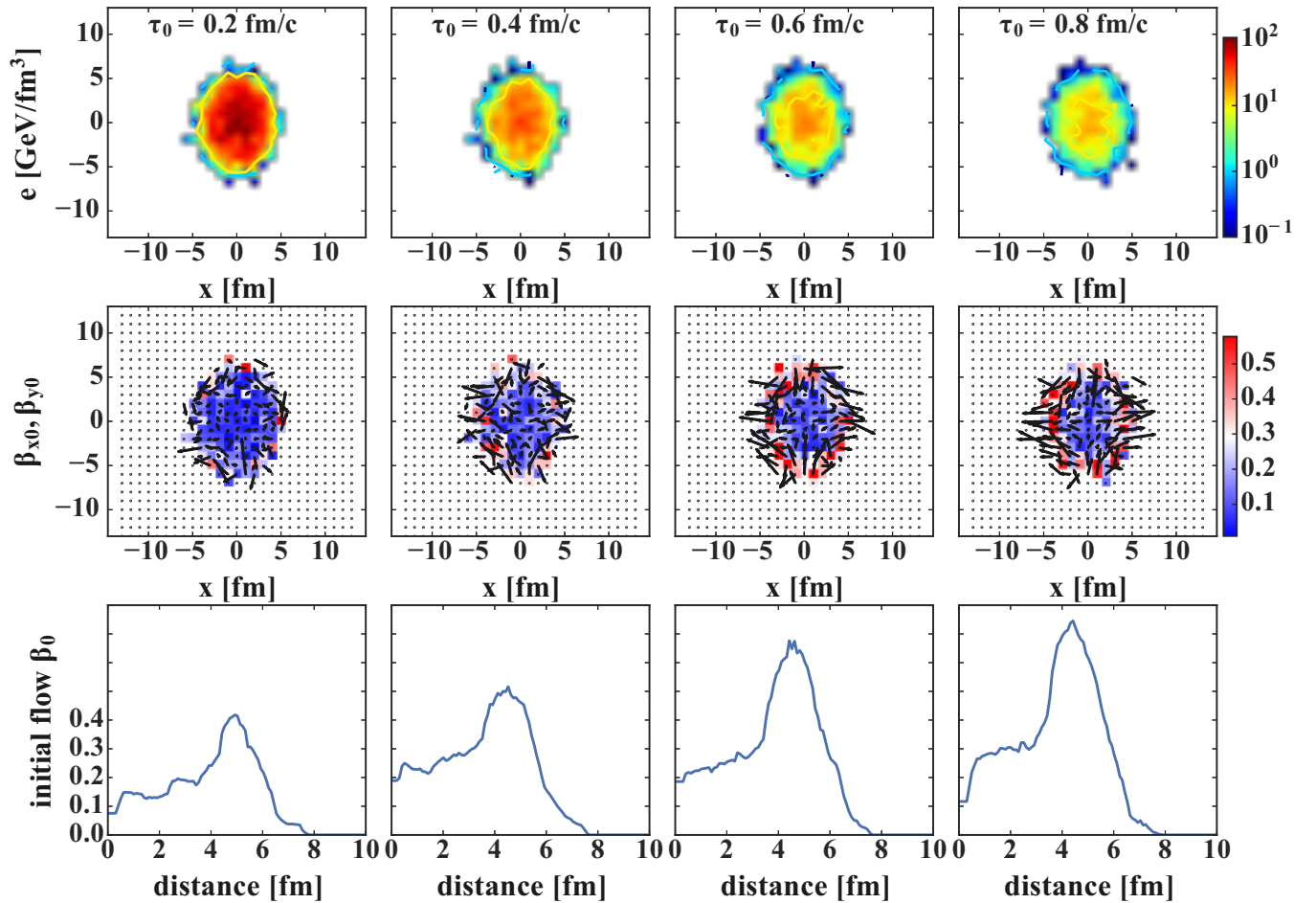


FIG. 2. Initial conditions of a peripheral Au+Au collision ( $b=6$  fm) at  $\sqrt{s_{NN}} = 200$  GeV (calculated within the PHSD). (Top contour) The local energy density in the transverse plane; (middle contour) quiver plot of initial flow  $v_x, v_y$  in the transverse plane (color map indicates the magnitude of local initial flow); (bottom contour) initial flow with respect to the distance of the cell from the center of energy density.

use (7) which gives us this set of equations:

$$\begin{aligned}
 (T^{00} - e) + T^{01}X + T^{02}Y + T^{03}Z &= 0, \\
 T^{10} + (T^{11} + e)X + T^{12}Y + T^{13}Z &= 0, \\
 T^{20} + T^{21}X + (T^{22} + e)Y + T^{23}Z &= 0, \\
 T^{30} + T^{31}X + T^{32}Y + (T^{33} + e)Z &= 0.
 \end{aligned} \quad (9)$$

Rearranging these equations, we can obtain the solutions which are actually for the vector  $u_\nu = \gamma (1, X, Y, Z) = \gamma (1, -\beta_x, -\beta_y, -\beta_z)$ . To obtain the physical 4-velocity  $u^\mu$ , we have to multiply by  $g^{\mu\nu}u_\nu = u^\mu$ .

### B. PHSD initial conditions for hydrodynamics

By the Landau matching procedure described above, we can obtain the initial conditions such as the local energy density  $e$  and initial flow  $\vec{\beta}$  for the hydrodynamical evolution. In the PHSD simulation the parallel ensemble algorithm is used for the test particle method, which has an impact on the fluctuating initial conditions. For a larger number of parallel ensembles (NUM), the energy density profile is smoother because it is calculated on the mean-field level by averaging over all ensembles. From a hydrodynamical point of view, gradients should not be too large and some smoothing of the initial conditions is therefore required. Here, we choose NUM = 30, which provides the same level of smoothing of the initial energy density as in typical PHSD simulations. In Fig. 1(a) we show the initial condition at time  $\tau = 0.6$  fm/c extracted from a single PHSD event averaged over (NUM = 30) parallel events, and averaged over 100 parallel events [Fig. 1(b)]; the color maps represent the local energy density while the arrows shows the initial flow at each of the cells. Even though the initial profiles are averaged over NUM = 30 parallel events, the distribution still captures the feature of event-by-event initial state fluctuations.

In Fig. 2 we investigate the dependence of the PHSD initial conditions on the equilibration time  $\tau_0$ , at which the nonequilibrium evolution is switched to a hydrodynamical evolution in local thermal equilibrium. As expected, for larger initial times  $\tau_0$ , the local initial flow increases and the local energy density decreases.

## IV. MEDIUM EVOLUTION: HYDRODYNAMICS VERSUS PHSD

In this section we compare the response of the hydrodynamical long-wavelength evolution to the PHSD initial conditions with the microscopic PHSD evolution itself. To avoid as many biases as possible we apply the temperature-dependent shear viscosity as determined in PHSD simulations [24] and shown in Fig. 3(a): The blue and red symbols correspond to  $\eta/s$  obtained from the Kubo formalism and from the relaxation time approximation method, respectively. As discussed in [24] the result agrees well also with the virial expansion approach [39]. The black line in Fig. 3 shows the parametrization of the PHSD  $\eta/s(T)$ , which is used in the viscous hydrodynamics for the present study. We note that the parametrized curve is very similar to the recently determined temperature dependence of

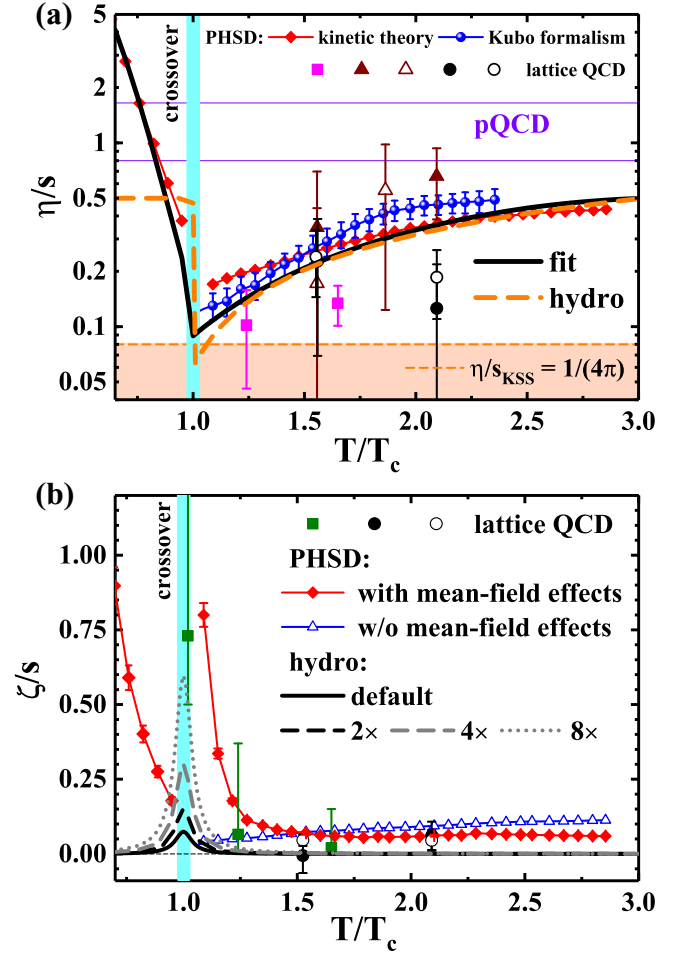


FIG. 3.  $\eta/s$  and  $\zeta/s$  versus scaled temperature  $T/T_c$ . (a) The symbols indicate the PHSD results of  $\eta/s$  from Ref. [24], calculated using different methods: the relaxation-time approximation (red line+diamonds) and the Kubo formalism (blue line+dots); the black line corresponds to the parametrization of the PHSD results for  $\eta/s$ . The orange short dashed line demonstrates the Kovtun-Son-Starinets bound [43] ( $\eta/s$ )<sub>KSS</sub> = 1/(4 $\pi$ ). The orange dashed line is the  $\eta/s$  of VISHNU hydrodynamical model that was recently determined by Bayesian analysis. (b)  $\zeta/s$  from PHSD simulations from Ref. [24] and the  $\zeta/s$  that is adapted in our hydrodynamical simulations.

$\eta/s$  via the Bayesian analysis of the available experimental data [40] (the orange dashed line).

While the effect of shear viscosity on the hydrodynamical evolution was studied extensively for simulations of heavy-ion collisions, bulk viscosity has not been treated as carefully so far. This is because at higher temperatures the bulk viscosity should be very small, and vanish in the conformal limit. Moreover, an enhanced bulk viscosity at the pseudocritical temperature causes problems for the applicability for hydrodynamics itself. Studies conducted for dynamical quasiparticle models, like the one used in PHSD, show that the magnitude and temperature behavior of the bulk viscosity depend on details of the parametrization of the equation of state and properties of the underlying degrees of freedom [22,24]. For the relaxation time approximation in quasiparticle models slightly different values for the bulk viscosity are obtained

[41,42]. Given these uncertainties for the values of the bulk viscosity, we decide to use the bulk viscosity that was recently determined by the Bayesian analysis of experimental data in our hydrodynamical simulations [40]. In Fig. 3(b) we compare the ratio of bulk viscosity to entropy  $\zeta/s$  that is adapted in our hydrodynamical simulations and the one extracted from PHSD simulations. It should be noted that the maximum  $\zeta/s$  that the hydrodynamical model can handle is much smaller than the bulk viscosity from PHSD simulations, and its effect on the momentum anisotropy will be discussed at the end of this section.

### A. Pressure isotropization

To justify the choice of initial time  $\tau_0 = 0.6$  fm, we first take a look at the evolution of the different pressure components in PHSD. In the pre-equilibrium stage deviations from thermal equilibrium are very large, however,  $(P_L + 2P_T)/e \approx 1$  up to  $0.15$  fm/c for all three panels. Without explicit representation we mention that for  $t > 0.15$  fm/c  $(P_L + 2P_T)/e$  is slightly lower than  $P/e$  from the EoS for some fm/c in case of the central cell and for  $x = 3$  fm, whereas both quantities are about equal for  $z = 5$  fm. This deviation we attribute to pre-equilibrium effects emerging in the PHSD calculations. According to common understanding one can apply hydrodynamics once the pressure is isotropic, which implies that both transverse and longitudinal pressure are about equal  $P_T \approx P_L$ .

As mentioned in the previous section, the deviations from equilibrium are strongest at the beginning of the heavy-ion collision. In this case the viscous corrections can have a large contribution to the energy-momentum tensor, and the pressure components can differ substantially from the isotropic pressure given by the EoS. This situation is illustrated in Fig. 4 which shows the evolution of the transverse and longitudinal pressures divided by the local energy density  $e$  in different cells along the  $x$  axis extracted from PHSD as a function of time for a peripheral Au+Au collision at  $\sqrt{s_{NN}} = 200$  GeV. These pressure components correspond to the eigenvalues of  $T^{\mu\nu}(x)$  where the latter have been averaged in this case over 100 PHSD events to get a smooth evolution. As seen from Fig. 4, at early reaction times the deviation between the pressure components is large and the longitudinal

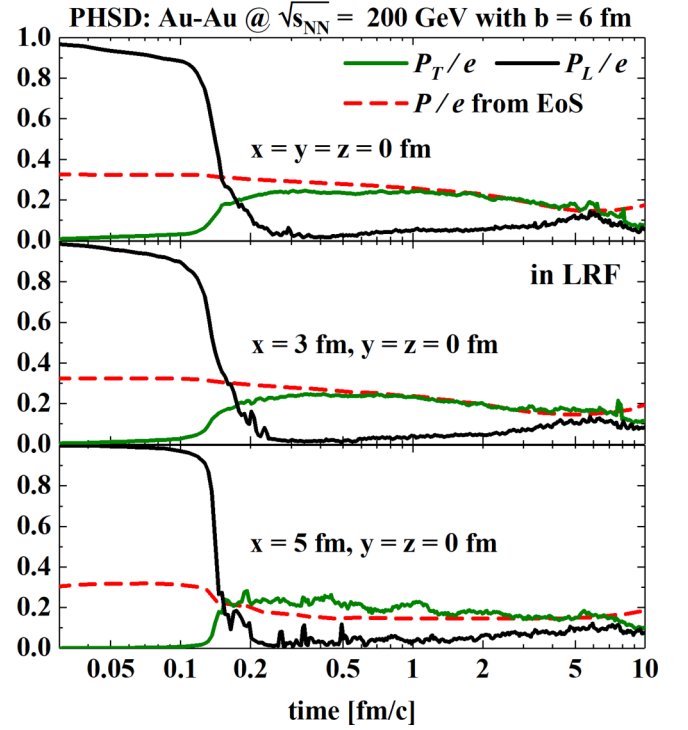


FIG. 4. Evolution of the ratio of the transverse  $P_T$  and longitudinal  $P_L$  pressures over the cell energy density  $e$  extracted from PHSD as a function of time for different cells along the  $x$  axis in a peripheral ( $b = 6$  fm) Au+Au collision at  $\sqrt{s_{NN}} = 200$  GeV. Note that  $T^{\mu\nu}$  was averaged over 100 PHSD events.

pressure dominates. The transverse pressure starts from zero but grows with time and approximately reaches the isotropic pressure within a range of 0.3–1 fm/c. On the other hand, the longitudinal pressure decreases to very low values and remains small for large times. One of the reasons for this behavior is that we took only a few cells on the  $z$  axis which correspond to a pseudorapidity gap  $\Delta\eta \approx \mathcal{O}(10^{-2})$ . By taking into account more cells in the longitudinal direction, the longitudinal pressure increases but the collective expansion cannot be removed properly in this case (as it was already studied in Sec. 7 of Ref. [13]). By looking at more peripheral

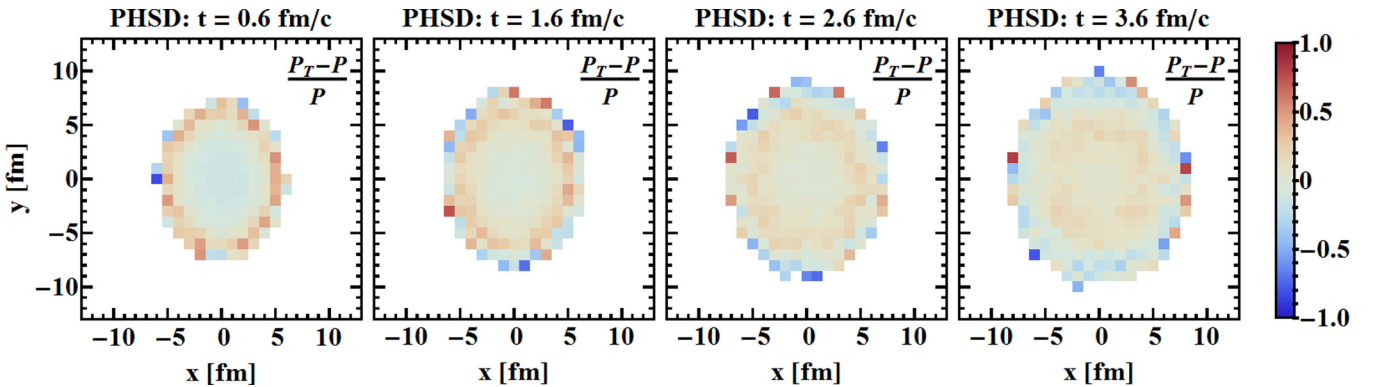


FIG. 5. Evolution of the relative value between the transverse pressure extracted from PHSD  $P_T$  (see also Fig. 4 for the pressure components) and the pressure  $P$  given by the EoS for different times in the transverse plane of a peripheral ( $b = 6$  fm) Au+Au collision at  $\sqrt{s_{NN}} = 200$  GeV. Note that  $T^{\mu\nu}$  was averaged over 100 PHSD events.

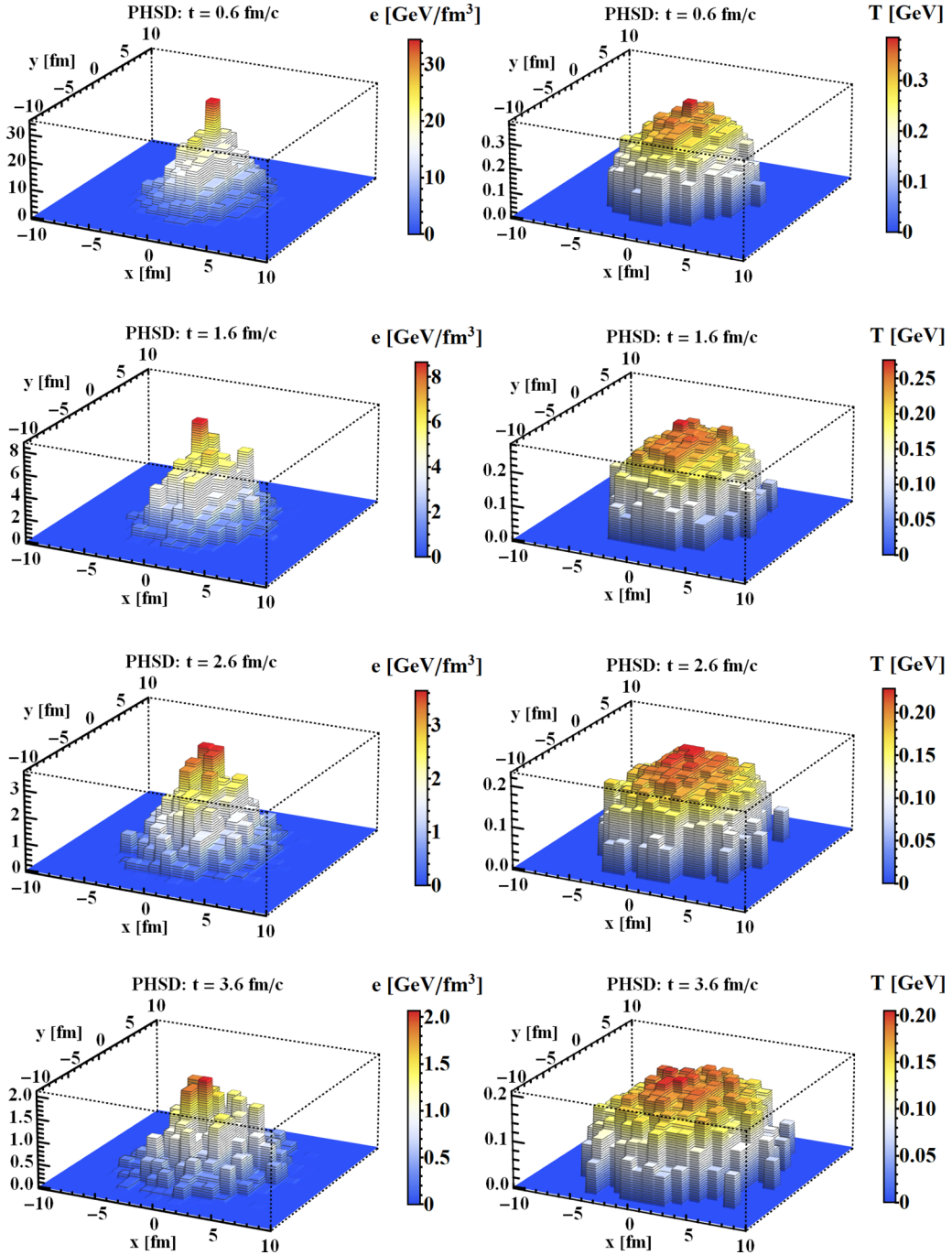


FIG. 6. Local energy density  $e(x, y, z = 0)$  (left column) and the corresponding temperature  $T(x, y, z = 0)$  given by the EoS (right column) in the transverse plane from a PHSD event (NUM = 30) at different times for a peripheral ( $b = 6$  fm) Au+Au collision at  $\sqrt{s_{NN}} = 200$  GeV.

cells (bottom panel of Fig. 4), we can see that the pressure components deviate more from the isotropic pressure given by the EoS compared to more central cells (top panel of Fig. 4).

We illustrate in Fig. 5 the (non-)equilibrated regions in the PHSD simulation. We evaluated the relative value between the transverse pressure extracted from PHSD  $P_T$  (see Fig. 4 for the pressure components) and the pressure  $P$  given by the EoS in the full transverse plane. One can see that the central region in gray is somewhat equilibrated for all times [ $(P_T - P)/P$  is around 0]. The peripheral cells have a higher pressure when the

initial condition for the hydrodynamical model is taken ( $t = 0.6$  fm/c), and then fluctuate around the isotropic pressure as depicted by the red and blue colors. We can therefore conclude that by averaging over the PHSD events, the medium reaches with time a transverse pressure comparable to the isotropic one as given by the IQCD EoS. This statement is of course not valid for a single PHSD event where the pressure components show a much more chaotic behavior and where the high fluctuations in density and velocity profiles indicate that the medium is in a nonequilibrium state, as we will see in the next section.

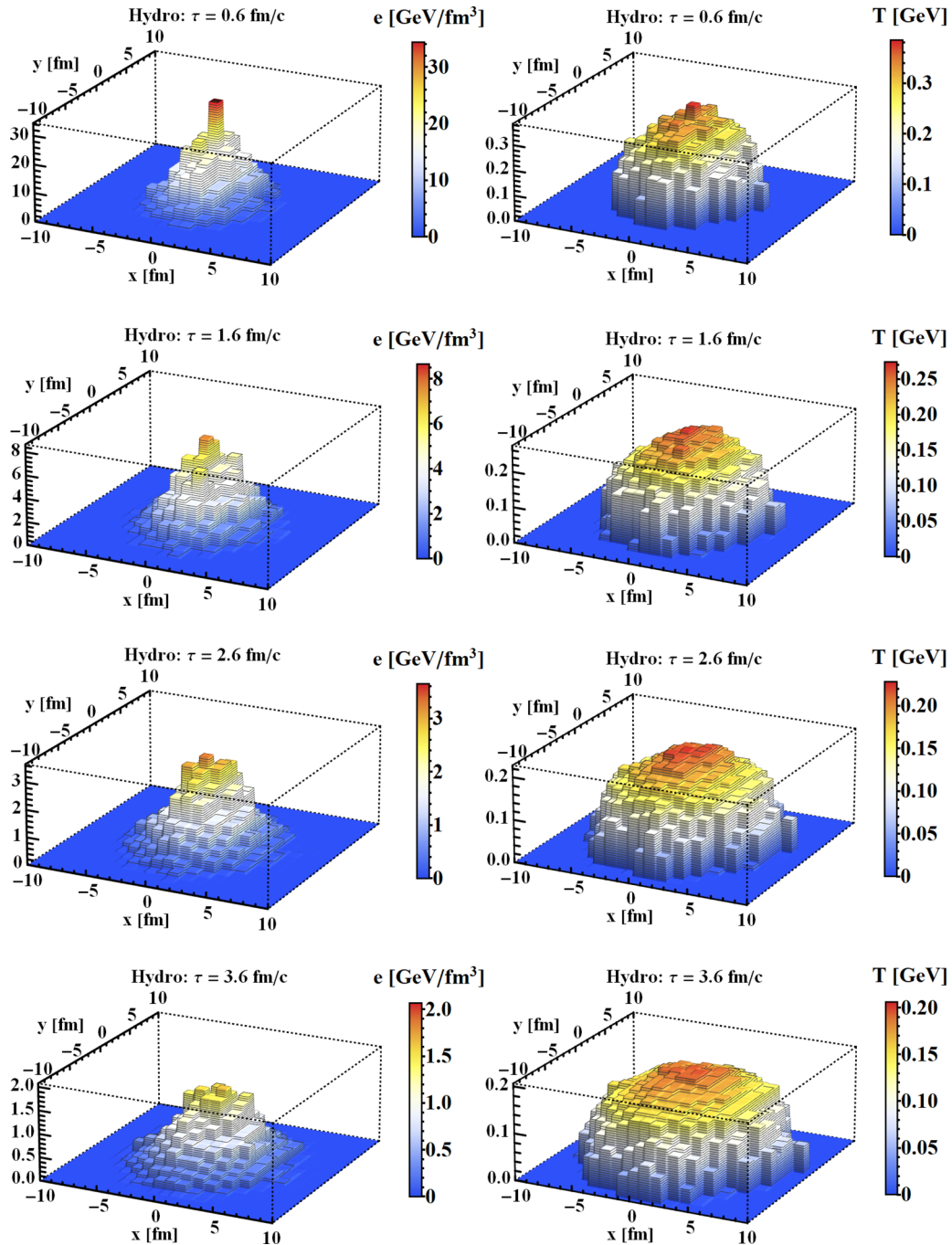


FIG. 7. Local energy density  $e(x, y, z = 0)$  (left column) and the corresponding temperature  $T(x, y, z = 0)$  given by the EoS (right column) in the transverse plane from a single hydrodynamical event at different proper times for a peripheral ( $b = 6$  fm) Au+Au collision at  $\sqrt{s_{NN}} = 200$  GeV.

### B. Space-time evolution of energy density $e$ and velocity $\bar{\beta}$

Starting with the same initial conditions (as discussed in Sec. III), the evolution of the QGP medium is now simulated by two different models: the nonequilibrium dynamics model (PHSD), and hydrodynamics, (2+1)-dimensional VISHNU.

Figure 6 shows the time evolution of the local energy density  $e(x, y, z = 0)$  (from  $T^{\mu\nu}$ ) (left) and the corresponding temperature  $T$  (right) as calculated using the IQCD EoS

in the transverse plane from a PHSD event (NUM = 30) at different times for a peripheral ( $b = 6$  fm) Au+Au collision at  $\sqrt{s_{NN}} = 200$  GeV. As seen in Fig. 1 for  $t = 0.6$  fm/c, the energy density profile is far from being smooth. Note also that the energy density decreases rapidly as the medium expands in the transverse and longitudinal direction. By converting the energy density to the temperature given by the IQCD EoS, we can see that the variations are less pronounced in that case. Figure 7 shows the same quantities for a single event evolved



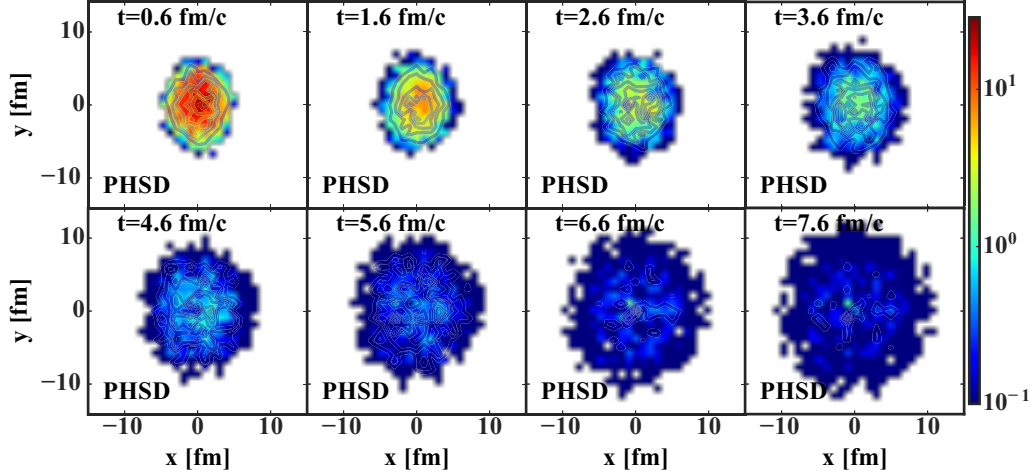


FIG. 8. Contour plots of the local energy density  $e$  in the transverse plane from the PHSD simulation of one event, for a peripheral Au+Au collision ( $b = 6$  fm) at  $\sqrt{s_{NN}} = 200$  GeV.

through hydrodynamics. In particular for the energy density at later times one can already observe a significant smoothing compared to the PHSD evolution.

Figure 8 shows the time evolution of the local energy density  $e(x, y)$  in the transverse plane from a single PHSD event (NUM=30) at different proper times for a peripheral Au+Au collision at  $\sqrt{s_{NN}} = 200$  GeV, while Fig. 9 shows the same time evolution of  $e(x, y)$  from a hydrodynamical evolution using the same initial condition as the PHSD event above. A comparison of the two medium evolutions shows distinct differences: In PHSD the energy density retains many small hot spots during its evolution because of its spatial nonuniformity. In hydrodynamics, the initial hot spots of energy density quickly dissolve and the medium becomes much smoother with increasing time. Moreover, as a result of the initial spatial anisotropy, the pressure gradient in the  $x$  direction is larger than that in the  $y$  direction, resulting in a slightly faster expansion in the  $x$  direction. We attribute these

differences directly to the nonequilibrium nature of the PHSD evolution.

In Figs. 10 and 11 we show the time evolution of the velocity  $\vec{\beta} = (\beta_x, \beta_y, \beta_z)$  in the transverse plane for the same PHSD initial condition evolved through PHSD and hydrodynamics. The longitudinal velocity  $\beta_z$  shown in the PHSD event remains on average approximately 0 and much smaller than the transverse flow because we only consider a narrow interval in the  $z$  direction. At  $\tau_0 = 0.6$  fm/c, transverse flow has already developed and the transverse velocity can reach values of 0.5 at the edge of the profile. Even though the velocity increases with time in both PHSD and hydrodynamical events, it is clearly seen that the development of flow in a hydrodynamical event is much faster than in a PHSD event. In addition, local fluctuations in a single event are more visible in the PHSD event. Moreover, the velocity in the  $x$  direction is slightly larger than the one in the  $y$  direction in both events, as a result of the initial spatial anisotropy of the energy density, and

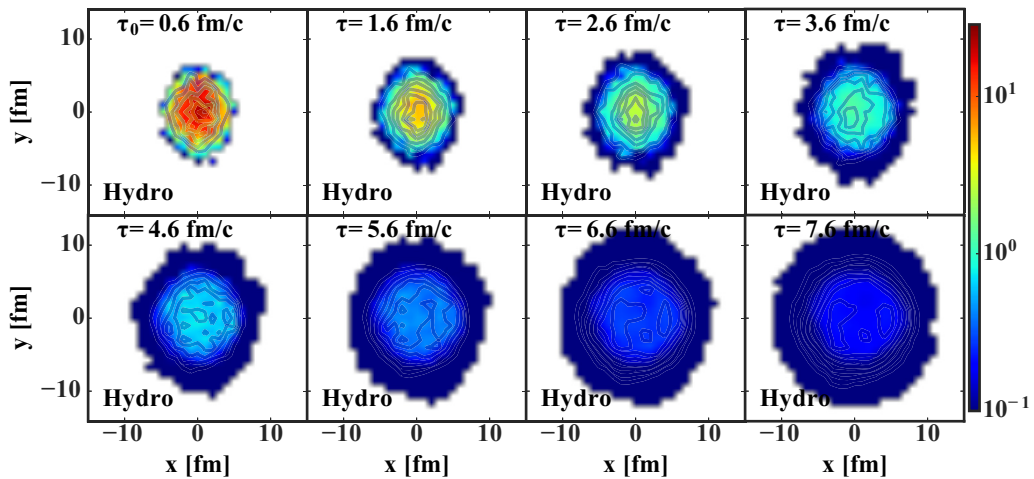


FIG. 9. Contour plots of the local energy density  $e$  in the transverse plane from the hydrodynamical simulation starting from the same initial conditions as in Fig. 8 including initial flow.

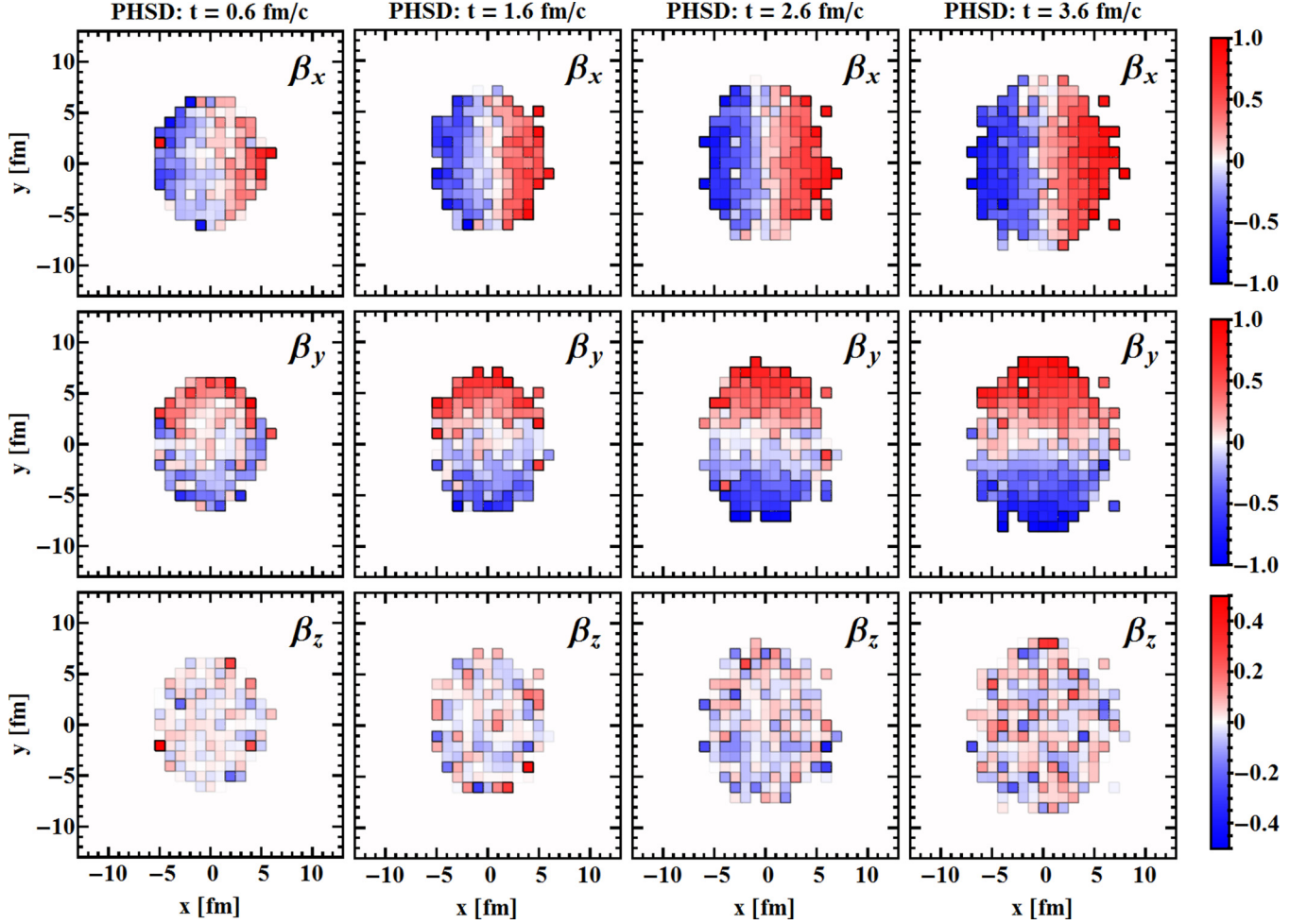


FIG. 10. Components of the 3-velocity ( $\beta_x, \beta_y, \beta_z$ ) in the transverse plane from a single PHSD event (NUM = 30) at a different proper time for a peripheral ( $b = 6$  fm) Au+Au collision at  $\sqrt{s_{NN}} = 200$  GeV.  $\beta_z$  is scaled differently from  $\beta_x, \beta_y$  for better orientation.

that spatial anisotropy is converted into momentum anisotropy, which increases with time.

### C. Fourier images of energy density

The inhomogeneity of a medium can be quantified by the Fourier transform of the energy density,  $\tilde{e}(k_x, k_y)$ . For a discrete spatial grid with an energy distribution as  $e(x, y)_{m \times n}$ , the Fourier coefficients are given by

$$\tilde{e}(k_x, k_y) = \frac{1}{m} \frac{1}{n} \sum_{x=0}^{m-1} \sum_{y=0}^{n-1} e(x, y) e^{2\pi i \left( \frac{xk_x}{m} + \frac{yk_y}{n} \right)}. \quad (10)$$

The zero mode  $\tilde{e}_{k_x=0, k_y=0}$  is the total sum of the energy density, while higher-order coefficients contain information about the correlations of the local energy density on different length scales. For a medium with large wave-length structures the higher-order coefficients should be suppressed and the typical global shape of the event should dominate. Given that our simulations in both PHSD and hydrodynamics are performed for the same centrality classes, we expect these structures to give similar Fourier coefficients for lower modes. However, if structures are dominated by smaller

length scales, the higher Fourier modes are excited as well.

In Figs. 12 and 13 we present the Fourier transform  $\tilde{e}(k_x, k_y)$  for a medium evolved by PHSD and hydrodynamics, respectively, for different stages of the evolution. For the hydrodynamical evolution of medium only the dominant lower Fourier modes survive in the later stages and shorter wavelength irregularities are washed out. The microscopic transport evolution of PHSD generates the same level of short wavelength phenomena at all times of the evolution; only the overall dilution of the medium reduces the strength.

This difference can be identified more easily in Fig. 14, where we plot the distribution of the Fourier coefficients  $\langle \tilde{e}(\sqrt{k_x^2 + k_y^2}) \rangle$  for different evolution times. For the lower order Fourier modes, which carry the information about the global event scale, the microscopically evolving medium and the hydrodynamical medium are practically identical. We observe that the strength of the shorter wavelength modes rapidly decreases with respect to the zero mode at the beginning of the hydrodynamical evolution. Higher-order Fourier modes survive in PHSD for longer times which should be attributed to dynamical fluctuations not incorporated in the present hydrodynamic calculations. Note that in

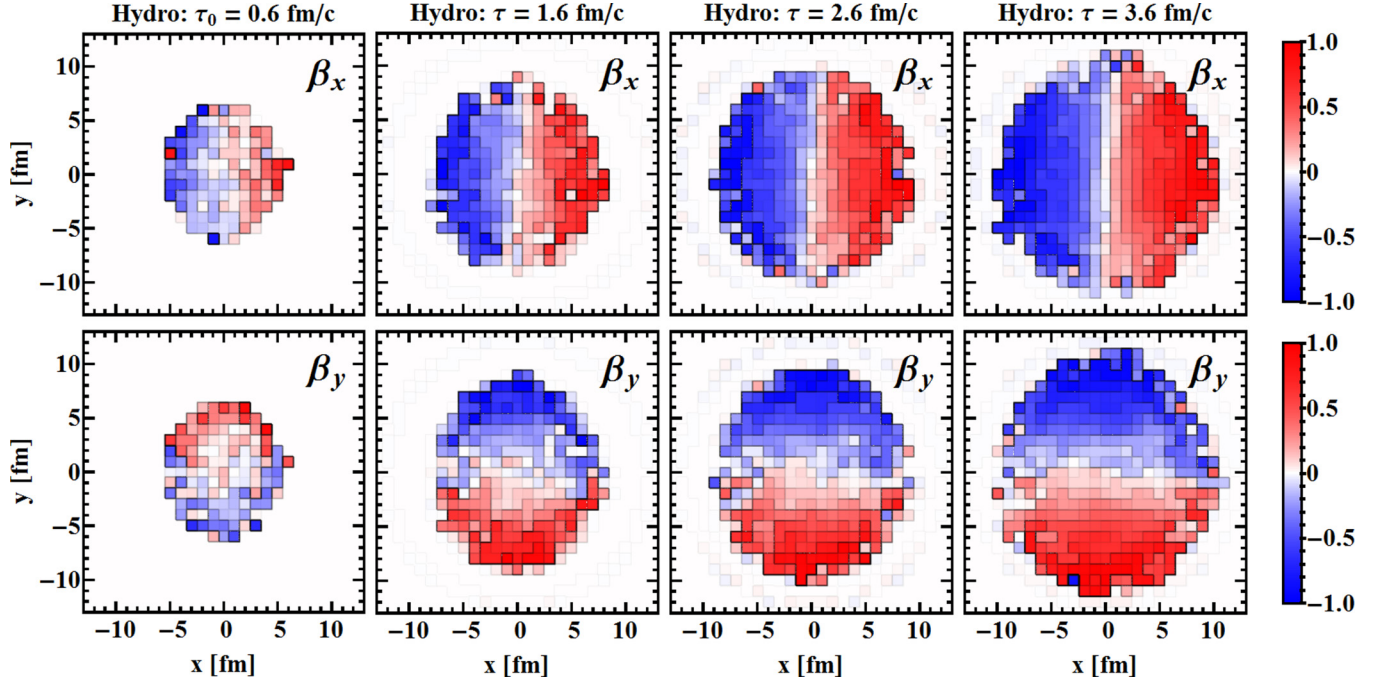


FIG. 11. Components of the velocity ( $\beta_x, \beta_y$ ) in the transverse plane from a single hydrodynamical event (taking the same initial condition as the PHSD event above) at a different proper time for a peripheral ( $b = 6$  fm) Au+Au collision at  $\sqrt{s_{NN}} = 200$  GeV.

thermodynamic equilibrium these fluctuations should not vanish according to the fluctuation-dissipation theorem (FDT) in case of a finite viscosity. In principle one might check within PHSD if the FDT holds in the late phase of the reaction, however, this question is beyond the scope of the present study. For a general formulation of hydrodynamics with dynamical fluctuations on the basis of the FDT we refer the reader to Ref. [44]. A numerical implementation [45] of linearized hydrodynamical fluctuations was studied in [46]. We note that a full numerical realization including the nonlinearities in the hydrodynamical equations is very challenging [47].

#### D. Time evolution of the spatial and momentum anisotropy

Much interest is given to the medium's response to initial spatial anisotropies. For the hydrodynamical models the spatial anisotropies lead to substantial collective flow, measured by Fourier coefficients of the azimuthal particle spectra. Initial spatial gradients are transformed into momentum anisotropies via hydrodynamical pressure. While experimentally only the final state particle spectra are known, models for the space-time evolution of the medium can give insight into the evolution of the spatial and the momentum anisotropy. For hydrodynamical models the latter is directly related to the elliptic flow  $v_2$ . Similar statements apply to the transport models where

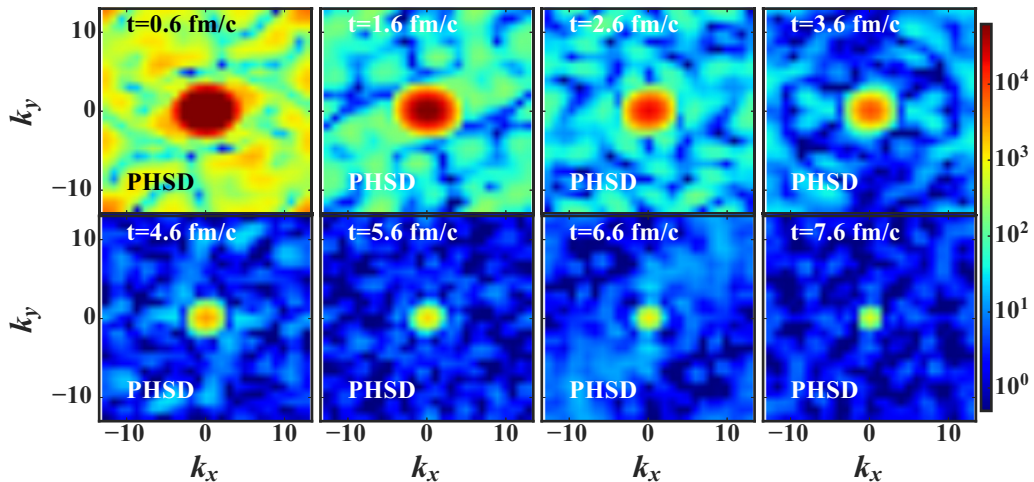


FIG. 12. Contour plots of the Fourier transform of the energy density  $\tilde{\epsilon}(x, y, z = 0)$  for the simulation obtained within PHSD as shown in Fig. 8.

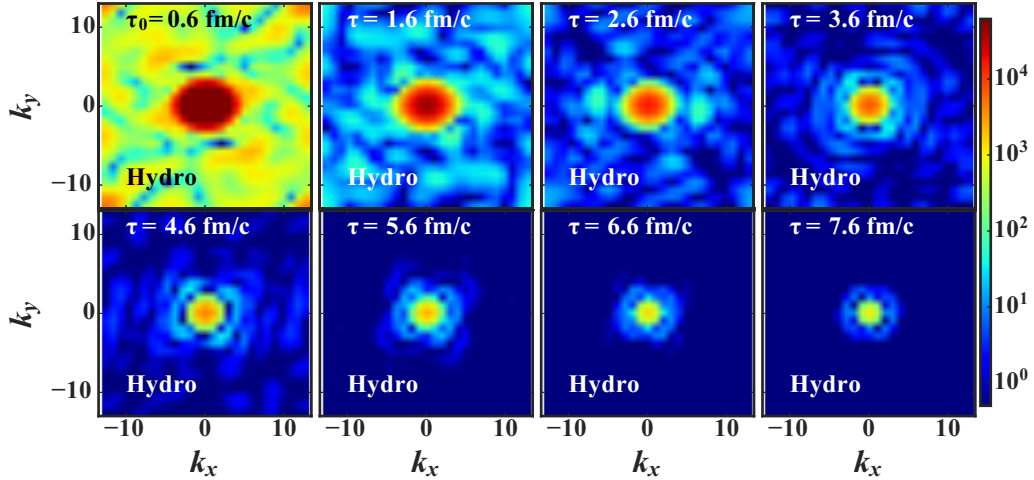


FIG. 13. Contour plots of the Fourier transform of the energy density  $\bar{e}(x, y, z = 0)$  for the simulation obtained within hydrodynamics as shown in Fig. 9.

the initial spatial anisotropies are converted to momentum anisotropies [8].

The spatial anisotropy of the matter distribution is quantified by the eccentricity coefficients  $\epsilon_n$  defined as

$$\epsilon_n \exp(in\Phi_n) = -\frac{\int r dr d\phi r^n \exp(in\phi) e(r, \phi)}{\int r dr d\phi r^n e(r, \phi)}, \quad (11)$$

where  $e(r, \phi)$  is the local energy density in the transverse plane.

The second-order coefficient  $\epsilon_2$  is also called ellipticity and to leading order the origin of the elliptic flow  $v_2$ . It can be simplified to

$$\epsilon_2 = \frac{\sqrt{\{r^2 \cos(2\phi)\}^2 + \{r^2 \sin(n\phi)\}^2}}{\{r^2\}}, \quad (12)$$

where  $\{\dots\} = \int dx dy (\dots) e(x, y)$  describes an event-averaged quantity weighted by the local energy density  $e(x, y)$  [48].

The importance of event-by-event fluctuations in the initial state was realized in particular for higher-order flow harmonics but also as a contribution to the elliptic flow and was extensively investigated both experimentally and theoretically [49–51]. As shown earlier, the PHSD model naturally produces initial state fluctuations because of its microscopic dynamics. We therefore apply event-by-event hydrodynamics and all subsequent quantities are averaged over many events.

In Fig. 15 we show the time evolution of the ellipticity  $\langle \epsilon_2 \rangle$  for both medium descriptions. For the PHSD simulations we observe large oscillations in  $\langle \epsilon_2 \rangle$  at the beginning of the evolution from the initialization geometries and formation times. After sufficient overlap of the colliding nuclei at the initial time

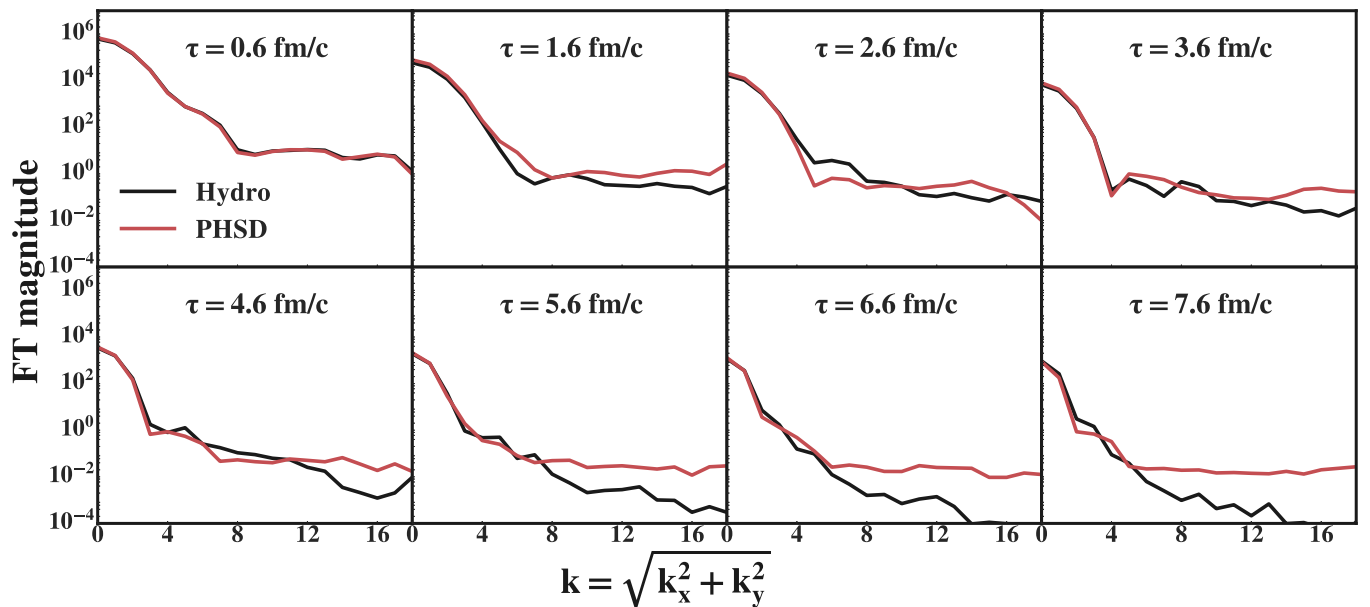


FIG. 14. Radial distribution of the Fourier modes of the energy density for a different proper time in both PHSD and hydrodynamical events. The red lines correspond to the PHSD simulations and the black line corresponds to the hydrodynamical simulations.

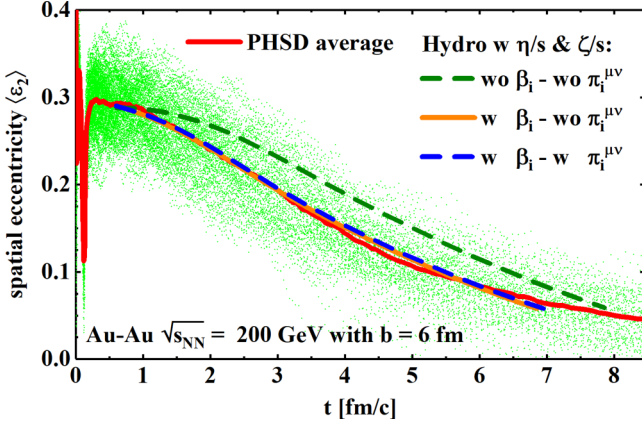


FIG. 15. Event-by-event averaged spatial eccentricity  $\langle \epsilon_2 \rangle$  of 100 PHSD events and 100 VISHNU events with respect to proper time, for a peripheral Au+Au collision ( $b = 6$  fm) at  $\sqrt{s_{NN}} = 200$  GeV. The green dots show the distribution of each of the 100 PHSD events used in this analysis. The solid red line is the average over all the green dots. The blue, yellow, and black lines correspond to hydrodynamical evolution taking different initial condition scenarios.

$\tau_0$  the average  $\langle \epsilon_2 \rangle$  is stabilized in PHSD. There are, however, still significant event-by-event fluctuations of this quantity at later times and strong variations between individual events.

In contrast, in a single hydrodynamical event  $\epsilon_p$  deviates from the average, but remains a smooth function of time. Because of the faster expansion in the  $x$  direction the initial spatial anisotropy decreases during the evolution for both medium descriptions. However, the spatial anisotropy decreases faster when initial pre-equilibrium flow  $\beta_i$  (extracted from the early PHSD evolution) is included in the hydrodynamical evolution. In this case, the time evolution of the event-by-event averaged spatial anisotropy is very similar in PHSD and in hydrodynamics. Initializing with the shear-stress tensor  $\pi_i^{\mu\nu}$

may have slight effects on the spatial eccentricity but not large enough to be visible.

A similar feature is also seen in the evolution of the momentum ellipticity, which is directly related to the integrated elliptic flow  $v_2$  of light hadrons. The total momentum ellipticity is determined from the energy-momentum tensor as [29,52]

$$\epsilon_p = \frac{\int dx dy (T^{xx} - T^{yy})}{\int dx dy (T^{xx} + T^{yy})}. \quad (13)$$

Here the energy-momentum tensor includes the viscous corrections from  $\pi^{\mu\nu}$  and  $\Pi$ .

In Fig. 16(a) we show the time evolution of the event-by-event averaged  $\langle \epsilon(p) \rangle$  for the hydrodynamical medium description with and without pre-equilibrium flow in the initial conditions. Including the initial flow leads to a finite momentum anisotropy at  $\tau_0$  which subsequently increases as the pressure transforms the spatial anisotropy in collective flow. Consequently,  $\epsilon_p$  is larger than in the scenario without initial flow throughout the entire evolution of the medium and an enhanced elliptic flow can be expected. Given the unresolved question of bulk viscosity in heavy-ion collisions, we investigate the effect of tuning the bulk viscosity from the standard value discussed at the beginning of this section to four times this value, which comes closer to the bulk viscosity found in different quasiparticle calculations [41,42]. We see that for an enhanced bulk viscosity around  $T_c$  the momentum anisotropy develops a bump at later times, which is more pronounced for larger bulk viscosity.

In Fig. 16(b) the hydrodynamical simulation is compared to the results from PHSD, again for event-by-event averaged quantities and the event-by-event fluctuations indicated by the spread of the cloud. The PHSD momentum eccentricity is constructed by Eq. (13) where  $T^{\mu\nu}$  is evaluated from Eq. (5). It can be observed that before  $\tau_0$  the averaged momentum anisotropy in PHSD develops continuously during the initial stage, before it reaches the value which is provided in the initial

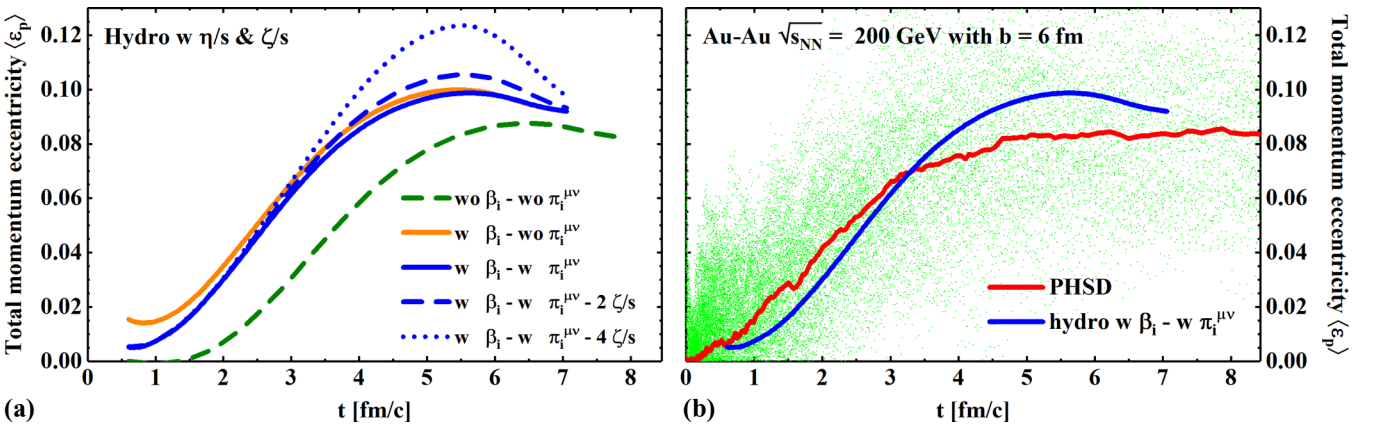


FIG. 16. Event-by-event averaged total momentum anisotropy of 100 PHSD events and 100 VISHNU events with respect to proper time, for a peripheral Au+Au collision ( $b = 6$  fm) at  $\sqrt{s_{NN}} = 200$  GeV. (a) The total momentum eccentricity of hydrodynamical evolution for different initial scenarios, as well as different bulk viscosity adapted in the hydrodynamical simulation. (b) Comparison of the total momentum eccentricity from PHSD events compared with the standard hydrodynamical events. The green dots show the distribution of each of the 100 PHSD events used in this analysis. The solid red line is an average over the green dots. The black line corresponds to the standard hydrodynamical evolution taking the 100 initial conditions which are generated from PHSD events.

conditions for hydrodynamics. Despite the seemingly large bulk viscosity, as discussed in the beginning of this section, the momentum anisotropy in PHSD does not show any hint of a bump like in the hydrodynamical calculation. The response to intrinsic bulk viscosity in a microscopic transport model does not seem to be as strong as in hydrodynamics.

## V. SUMMARY

In this paper, we have compared two commonly used descriptions of the evolution of a QGP medium in heavy-ion collisions, the microscopic off-shell transport approach PHSD and a macroscopic hydrodynamical evolution. Both approaches give an excellent agreement with numerous experimental data, despite the very different assumptions inherent in these models. In PHSD, quasiparticles are treated in off-shell transport with thermal masses and widths which reproduce the lattice QCD equation of state and are determined from parallel event runs in the simulations. Hydrodynamics assumes local equilibrium to be reached in the initial stages of heavy-ion collisions and transports energy-momentum and charge densities according to the lattice QCD equation of state and transport coefficients such as the shear and bulk viscosity. We have tried to match the hydrodynamical evolution as closely as possible to these quantities as obtained within PHSD.

- (1) By construction the equation of state in PHSD is compatible with the IQCD equation of state used in the hydrodynamical evolution.
- (2) A new Landau-matching procedure was used to determine initial conditions for hydrodynamics from the PHSD simulation.
- (3) The hydrodynamical simulations utilize the same  $\eta/s(T)$  as obtained within PHSD.
- (4) Different bulk viscosity parametrizations have been introduced in the hydrodynamical simulation that resemble those obtained in (dynamical) quasiparticle models, which are the basis for PHSD simulations.

In general we find that the ensemble averages over PHSD events follow closely the hydrodynamical evolution. The major

differences between the macroscopic near-(local)-equilibrium and the microscopic off-equilibrium dynamics can be summarized as the following.

- (1) A strong short-wavelength spatial irregularity in PHSD at all times during the evolution versus a fast smoothing of initial irregularities in the hydrodynamical evolution such that only global long-wavelength structures survive. These structures have been calculated on the level of the fluid velocity and energy density and quantified in terms of the Fourier modes of the energy density. Because of the QCD equation of state the irregularities imprinted in the temperature are smaller than in the energy density itself.
- (2) The hydrodynamical response to changing transport coefficients, especially the bulk viscosity, has a strong impact on the time evolution of the momentum anisotropy. In PHSD these transport coefficients can be determined but remain intrinsically linked to the interaction cross sections. Although there are indications for a substantial bulk viscosity in PHSD, it does not show the same sensitivity to the momentum space anisotropy as in hydrodynamical simulations.
- (3) Event-by-event fluctuations might be of similar magnitude in quantities like the spatial and momentum anisotropy but while they remain smooth functions of time in hydrodynamics significant variations are observed within a single event in PHSD as a function of time.

After having gained an improved understanding of the similarities and differences in the evolution of bulk QCD matter between the nonequilibrium PHSD and the equilibrium hydrodynamic approach, we plan to utilize our insights in future projects regarding the development of observables sensitive to nonequilibrium effects and the impact these effects may have on hard probe observables.

## ACKNOWLEDGMENTS

We appreciate fruitful discussions with J. Aichelin, W. Cassing, P.-B. Gossiaux, and T. Kodama. This work in part was supported by the LOEWE center HIC for FAIR as well as by BMBF and DAAD. The computational resources have been provided by the LOEWE-CSC. S.A.B., M.G., and Y.X. acknowledge support by the U.S. Department of Energy under Grant No. DE-FG02-05ER41367.

## APPENDIX

### 1. Fourier transform of energy density

For a discrete 2D Fourier transform, we have

$$\tilde{X}(k,l) = \sum_{m=0}^{M-1} \sum_{n=0}^{N-1} x(m,n) e^{-2\pi i \frac{mk}{M}} e^{-2\pi i \frac{nl}{N}}, \quad (\text{A1})$$

$$x(m,n) = \frac{1}{MN} \sum_{m=0}^{M-1} \sum_{n=0}^{N-1} \tilde{X}(k,l) e^{2\pi i (\frac{mk}{M} + \frac{nl}{N})} \quad (\text{A2})$$

$$= \frac{1}{MN} \sum_{m=0}^{M-1} \sum_{n=0}^{N-1} \tilde{X}(k,l) \left[ \cos \left( 2\pi \left( \frac{mk}{M} + \frac{nl}{N} \right) \right) + i \sin \left( 2\pi \left( \frac{mk}{M} + \frac{nl}{N} \right) \right) \right] \quad (\text{A3})$$

$$= \frac{1}{MN} \sum_{m=0}^{M-1} \sum_{n=0}^{N-1} \left[ \tilde{X}_{\text{real}}(k,l) \cos \left( 2\pi \left( \frac{mk}{M} + \frac{nl}{N} \right) \right) - \tilde{X}_{\text{imag}}(k,l) \sin \left( 2\pi \left( \frac{mk}{M} + \frac{nl}{N} \right) \right) \right]. \quad (\text{A4})$$

$\tilde{X}_{\text{real}}$  and  $\tilde{X}_{\text{imag}}$  are the real and imaginary part of Fourier transform coefficients  $\tilde{X}$ ,

$$\tilde{X}_{\text{real}}(k,l) = \sum_{m=0}^{M-1} \sum_{n=0}^{N-1} x(m,n) \cos \left( 2\pi \left( \frac{mk}{M} + \frac{nl}{N} \right) \right), \quad (\text{A5})$$

$$\tilde{X}_{\text{imag}}(k,l) = - \sum_{m=0}^{M-1} \sum_{n=0}^{N-1} x(m,n) \sin \left( 2\pi \left( \frac{mk}{M} + \frac{nl}{N} \right) \right). \quad (\text{A6})$$

Therefore,  $FT$  is defined as

$$|\tilde{X}(k,l)|^2 = |\tilde{X}_{\text{real}}(k,l)|^2 + |\tilde{X}_{\text{imag}}(k,l)|^2 \quad (\text{A7})$$

$$= \sum_{m=0}^{M-1} \sum_{n=0}^{N-1} x^2(m,n) \quad (\text{A8})$$

$$+ \sum_{m \neq m', n \neq n'} x(m,n)x(m',n'), \quad (\text{A9})$$

$$\cos \left( 2\pi \left( \frac{(m-m')k}{M} + \frac{(n-n')l}{N} \right) \right). \quad (\text{A10})$$

- [1] I. Arsene *et al.* (BRAHMS Collaboration), *Nucl. Phys. A* **757**, 1 (2005).
- [2] K. Adcox *et al.* (PHENIX Collaboration), *Nucl. Phys. A* **757**, 184 (2005).
- [3] B. B. Back *et al.*, *Nucl. Phys. A* **757**, 28 (2005).
- [4] J. Adams *et al.* (STAR Collaboration), *Nucl. Phys. A* **757**, 102 (2005).
- [5] M. Gyulassy and L. McLerran, *Nucl. Phys. A* **750**, 30 (2005).
- [6] B. Müller and J. L. Nagle, *Ann. Rev. Nucl. Part. Sci.* **56**, 93 (2006).
- [7] B. Müller, J. Schukraft, and B. Wyslouch, *Ann. Rev. Nucl. Part. Sci.* **62**, 361 (2012).
- [8] W. Cassing and E. L. Bratkovskaya, *Phys. Rev. C* **78**, 034919 (2008).
- [9] W. Cassing and E. L. Bratkovskaya, *Nucl. Phys. A* **831**, 215 (2009).
- [10] E. L. Bratkovskaya, W. Cassing, V. P. Konchakovski, and O. Linnyk, *Nucl. Phys. A* **856**, 162 (2011).
- [11] H. Song and U. W. Heinz, *Phys. Rev. C* **77**, 064901 (2008).
- [12] C. Shen, Z. Qiu, H. Song, J. Bernhard, S. Bass, and U. Heinz, *Comput. Phys. Commun.* **199**, 61 (2016).
- [13] R. Derradi de Souza, T. Koide, and T. Kodama, *Prog. Part. Nucl. Phys.* **86**, 35 (2016).
- [14] R. D. de Souza, J. Takahashi, T. Kodama, and P. Sorensen, *Phys. Rev. C* **85**, 054909 (2012).
- [15] H. Niemi, G. S. Denicol, H. Holopainen, and P. Huovinen, *Phys. Rev. C* **87**, 054901 (2013).
- [16] S. A. Voloshin *et al.*, *J. Phys. G* **34**, S883 (2007).
- [17] V. P. Konchakovski, W. Cassing, and V. D. Toneev, *J. Phys. G* **41**, 105004 (2014).
- [18] W. Cassing, *Eur. Phys. J. ST* **168**, 3 (2009); *Nucl. Phys. A* **795**, 70 (2007).
- [19] L. P. Kadanoff and G. Baym, *Quantum Statistical Mechanics* (Benjamin, New York, 1962).
- [20] S. Juchem, W. Cassing, and C. Greiner, *Phys. Rev. D* **69**, 025006 (2004); *Nucl. Phys. A* **743**, 92 (2004).
- [21] W. Cassing and E. L. Bratkovskaya, *Phys. Rep.* **308**, 65 (1999); W. Cassing, E. L. Bratkovskaya, and S. Juchem, *Nucl. Phys. A* **674**, 249 (2000).
- [22] H. Berrehrah, E. Bratkovskaya, T. Steinert, and W. Cassing, *Int. J. Mod. Phys. E* **25**, 1642003 (2016).
- [23] V. Ozvenchuk, O. Linnyk, M. I. Gorenstein, E. L. Bratkovskaya, and W. Cassing, *Phys. Rev. C* **87**, 024901 (2013).
- [24] V. Ozvenchuk, O. Linnyk, M. I. Gorenstein, E. L. Bratkovskaya, and W. Cassing, *Phys. Rev. C* **87**, 064903 (2013).
- [25] W. Cassing, O. Linnyk, T. Steinert, and V. Ozvenchuk, *Phys. Rev. Lett.* **110**, 182301 (2013); T. Steinert and W. Cassing, *Phys. Rev. C* **89**, 035203 (2014).
- [26] B. Andersson, G. Gustafson, and H. Pi, *Z. Phys. C* **57**, 485 (1993).
- [27] V. P. Konchakovski *et al.*, *J. Phys. G* **42**, 055106 (2015); V. P. Konchakovski, *Phys. Rev. C* **85**, 044922 (2012); **85**, 011902 (2012); **90**, 014903 (2014).
- [28] O. Linnyk, E. L. Bratkovskaya, and W. Cassing, *Prog. Part. Nucl. Phys.* **87**, 50 (2016).
- [29] J. Liu, C. Shen, and U. Heinz, *Phys. Rev. C* **91**, 064906 (2015); **92**, 049904 (2015).
- [30] W. Israel and J. M. Stewart, *Annals. Phys.* **118**, 341 (1979).
- [31] W. Israel and J. M. Stewart, *Phys. Lett. A* **58**, 4 (1976).

- [32] G. S. Denicol, S. Jeon, and C. Gale, *Phys. Rev. C* **90**, 024912 (2014).
- [33] A. Bazavov *et al.* (HotQCD Collaboration), *Phys. Rev. D* **90**, 094503 (2014).
- [34] J. S. Moreland and R. A. Soltz, *Phys. Rev. C* **93**, 044913 (2016).
- [35] B. Schenke, P. Tribedy, and R. Venugopalan, *Phys. Rev. Lett.* **108**, 252301 (2012).
- [36] A. Adil, H.-J. Drescher, A. Dumitru, A. Hayashigaki, and Y. Nara, *Phys. Rev. C* **74**, 044905 (2006).
- [37] M. L. Miller, K. Reygers, S. J. Sanders, and P. Steinberg, *Ann. Rev. Nucl. Part. Sci.* **57**, 205 (2007).
- [38] J. S. Moreland, J. E. Bernhard, and S. A. Bass, *Phys. Rev. C* **92**, 011901 (2015).
- [39] S. Mattiello and W. Cassing, *Eur. Phys. J. C* **70**, 243 (2010).
- [40] J. Bernhard *et al.*, Quark Matter 2017 [<https://indico.cern.ch/event/433345/contributions/2358284/>].
- [41] C. Sasaki and K. Redlich, *Phys. Rev. C* **79**, 055207 (2009).
- [42] M. Bluhm, B. Kämpfer, and K. Redlich, *Phys. Rev. C* **84**, 025201 (2011).
- [43] G. Policastro, D. T. Son, and A. O. Starinets, *Phys. Rev. Lett.* **87**, 081601 (2001); P. K. Kovtun, D. T. Son, and A. O. Starinets, *ibid.* **94**, 111601 (2005).
- [44] J. I. Kapusta, B. Müller, and M. Stephanov, *Phys. Rev. C* **85**, 054906 (2012).
- [45] C. Young, *Phys. Rev. C* **89**, 024913 (2014).
- [46] C. Young, J. I. Kapusta, C. Gale, S. Jeon, and B. Schenke, *Phys. Rev. C* **91**, 044901 (2015).
- [47] M. Nahrgang, M. Bluhm, T. Schfer, and S. Bass, [arXiv:1704.3553](https://arxiv.org/abs/1704.3553).
- [48] Z. Qiu and U. W. Heinz, *Phys. Rev. C* **84**, 024911 (2011).
- [49] M. Miller and R. Snellings, [arXiv:cond-mat/0312008](https://arxiv.org/abs/cond-mat/0312008).
- [50] B. Alver *et al.* (PHOBOS Collaboration), *Phys. Rev. Lett.* **98**, 242302 (2007).
- [51] B. Alver and G. Roland, *Phys. Rev. C* **81**, 054905 (2010); **82**, 039903 (2010).
- [52] P. F. Kolb and U. W. Heinz, *Quark Gluon Plasma 3*, edited by R. C. Hwa and X.-N. Wang (World Scientific, Singapore, 2004), pp. 634–714.